Research Square

Preprints are preliminary reports that have not undergone peer review.
They should not be considered conclusive, used to inform clinical practice,
or referenced by the media as validated information.

Heisenberg Distributed Acoustic Sensing Realized on Commercial Optical Communication Terminals

Bo Wang

bo.wang@tsinghua.edu.cn

Tsinghua University https://orcid.org/0000-0002-2918-1912

Zhongwang Pang

Tsinghua University https://orcid.org/0000-0002-8810-9531

Chunyi Li

Tsinghua University

Dongqi Song

Tsinghua University https://orcid.org/0009-0003-5171-963X

Wenlin Li

Tsinghua University https://orcid.org/0000-0003-0887-4100

Tong Wu

Tsinghua University

Hao Zhu

Tsinghua University

Peijian Sun

Tsinghua University

Article

Keywords:

Posted Date: June 23rd, 2026

DOI: https://doi.org/10.21203/rs.3.rs-9904347/v1

License: This work is licensed under a Creative Commons Attribution 4.0 International License.
Read Full License

Additional Declarations: There is **NO** Competing Interest.

Title: Heisenberg Distributed Acoustic Sensing Realized on Commercial Optical Communication Terminals

Zhongwang Pang,[1,2, †] Chunyi Li,[1,2, †] Dongqi Song,[1,2] Wenlin Li,[1,2] Tong Wu,[1,2] Hao Zhu,[1,2] Peijian Sun,[1,2] and Bo Wang[1,2, *]

1. State Key Laboratory of Precision Space-time Information Sensing Technology, Department of Precision Instrument, Tsinghua University, Beijing, China, 100084

2. Key Laboratory of Photonic Control Technology (Tsinghua University), Ministry of Education, Beijing, China, 100084

†These authors contributed equally to this paper.

E-mail: bo.wang@tsinghua.edu.cn

Abstract

The integration of communication and sensing can transform fiber-optic communication networks into sensing infrastructure. However, conventional distributed acoustic sensing (DAS) relies on narrow-linewidth pulsed probe light and is therefore generally considered incompatible with deployed communication systems. Here, based on the Heisenberg uncertainty principle, we show that continuous-wave communication light from a commercial small form-factor pluggable (SFP) optical transceiver can directly serve as the sensing light for DAS, without perturbing live communication services. Experiments reveal an uncertainty relation between spatial resolution and laser frequency uncertainty, with broader laser linewidth yielding finer spatial resolution. We further validate the system on a live commercial communication link by monitoring high-speed trains, without modifying the communication terminals, or launching additional probe light. This study points to broad opportunities for large-scale sensing on global fiber communication network.

Introduction

Optical communication cables can serve as large-scale distributed sensing media, enabling extensive monitoring of submarine earthquakes[1-3], land transportation[4,5], volcanic activity[6-9], and glacier dynamics[10-12]. These advancements are paving the way for the global fiber network to evolve into a planetary-scale nervous system capable of sensing both human and geophysical activities[13-17]. However, a fundamental gap exists between fiber communication and distributed fiber sensing: their optical signals are intrinsically different, which prevents seamless integration[18]. Conventional communication light, such as that from a standard Small Form-factor Pluggable (SFP) optical transceiver, cannot be directly applied to distributed sensing. Communication systems typically employ continuous-wave (CW) light with data encoded via intensity or phase modulation. In contrast, as a representative technology of distributed fiber sensing, distributed acoustic sensing (DAS) relies on narrow optical pulses as probe signals. Its spatial resolution ΔL is related to the pulse width Δt by $\Delta L = v_n \Delta t/2$ [19,20], where v_n is the velocity of light in the fiber. Shorter pulses offer superior spatial resolution[21-23]. To integrate communication and sensing, previous studies have utilized multiplexing techniques (in time, wavelength, or frequency domain) to create dual-purpose light that carries both data and sensing information over the same fiber[18,24-26]. However, these techniques usually require modifications to the light source or modulation/demodulation schemes, often at the expense of temporal or spectral resources[18]. Whether the communication light itself can directly serve as a sensing resource remains a question of substantial interest[27,28].

Since its introduction by Heisenberg in 1927, the uncertainty principle and its extensions have driven progress in many fields, including gravitational-wave detection[29,30], quantum computing[31,32], quantum key distribution[33], and the analysis of electroencephalography and acoustic signals[34-36], as illustrated in Fig. 1a. The position-momentum uncertainty relation, $\Delta x \cdot \Delta p \geq \hbar/2$, provides a spatial resolution limit distinct from the classical view ($\Delta L = v_n \Delta t/2$) of conventional DAS. For a photon with momentum uncertainty $\Delta p = \Delta(h/\lambda) = h\Delta\nu/v_n$, this relation gives $\Delta x \cdot \Delta \nu \geq v_n/4\pi$, where λ is the laser wavelength and ν is its frequency. Thus, a larger photon momentum uncertainty Δp (or laser frequency uncertainty $\Delta \nu$) allows

a smaller position uncertainty Δx, implying a superior theoretical limit on spatial resolution in optical fiber sensing.

In this work, inspired by the Heisenberg uncertainty principle, we propose Heisenberg distributed acoustic sensing (H-DAS). It relies on the properties of photons, whereby a wider laser linewidth yields superior sensing spatial resolution. This constitutes a key distinction from classical distributed fiber sensing mechanisms. A low-cost broadband CW light source, SFP module of commercial optical communication terminal, is directly deployed as sensing light source for H-DAS. We experimentally demonstrate the uncertainty relation between sensing spatial resolution and laser frequency uncertainty, and achieve a 25-cm sensing spatial resolution using a commercial SFP module operating at 1.25 Gbps. The distributed sensing capability of H-DAS is validated in a 12-km field trial along the Beijing-Guangzhou high-speed railway. By reusing existing track-side fiber and commercial optical communication terminals, the system achieves real-time sensing and localization of operating trains. These results provide a practical route toward realizing a plug-and-play, large-scale fiber communication and sensing network envisioned in Fig. 1a.

Results

Using communication light for distributed sensing

As discussed above, conventional DAS system typically uses optical pulse from the narrow-linewidth laser as the sensing light. By contrast, laser in communication system usually exhibits broad linewidth (>10 MHz) and operates in CW mode, which makes it unsuitable for direct use in DAS. From a photon-based perspective, as depicted in Fig. 1b, the CW light from such a broadband source can be conceptualized as a sequence of photon packets with short coherence length. Taken the red photon packet as an example, photons (illustrated by small spheres) within it are mutually coherent, and the packet has a spatial length of approximately $2\Delta x$. Photon packets separated by more than $2\Delta x$ are statistically incoherent. For a laser with 10 MHz full width at half maximum (FWHM) in frequency, using $FWHM = 2\sqrt{2\ln 2}\Delta\nu$ [37,38], we obtain $\Delta x \geq \frac{v_n}{4\pi \cdot \Delta\nu} \approx 37$ m.

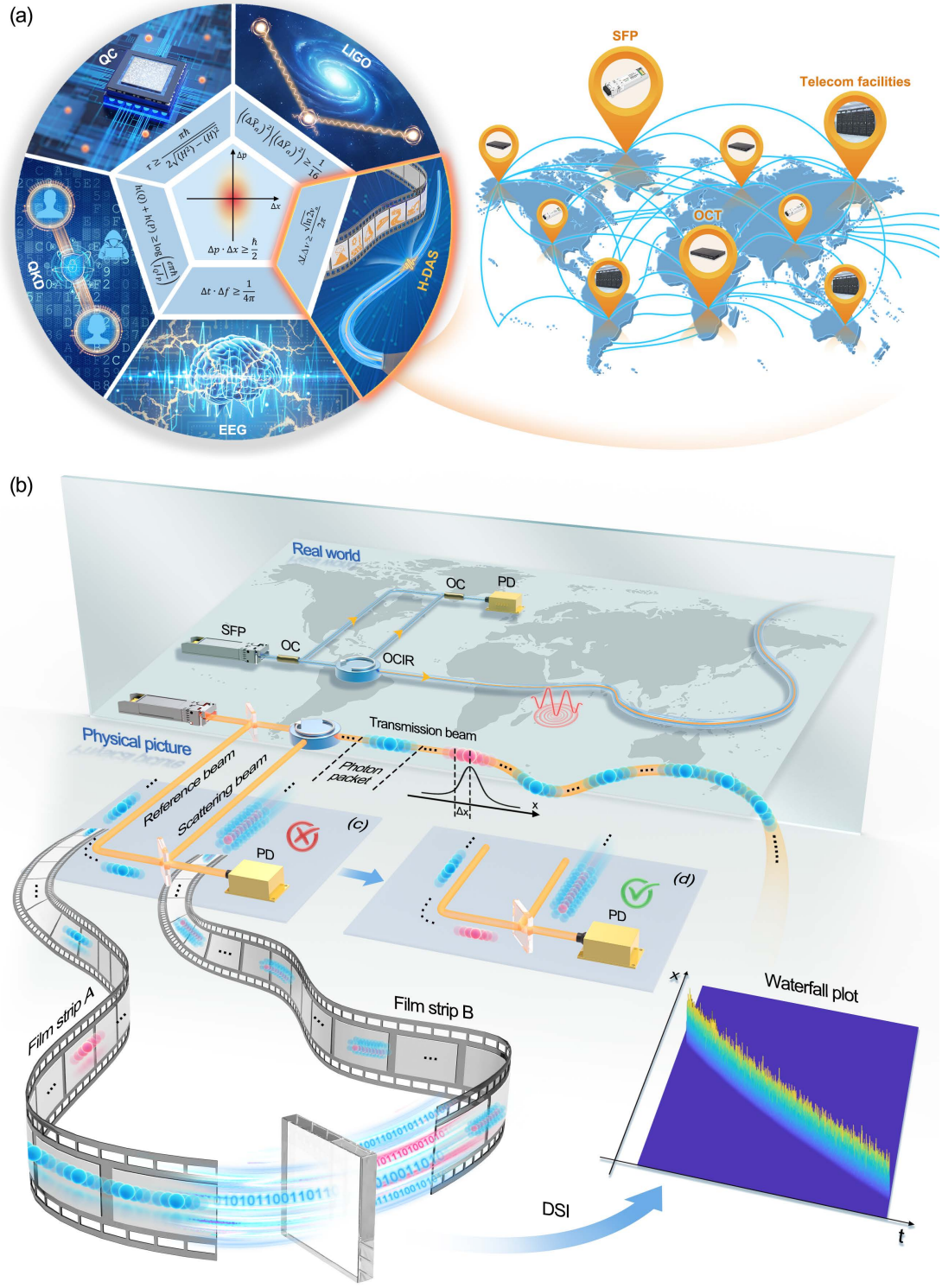


Fig. 1 | Principle and detection mechanism of H-DAS. a, Extensions and applications of the Heisenberg uncertainty principle. In particular, H-DAS is expected to add a plug-and-play distributed sensing capability to global communication networks by reusing existing telecom infrastructure (SFPs, OCTs and telecom facilities). **b,** System schematic and physical picture. The panel is conceptually divided into “real world” and

corresponding “physical picture”, separated by a “mirror”. In the real world side, an SFP optical transceiver launches broadband CW light into the fiber link. In its physical picture side, this CW transmission beam can be viewed as a sequence of photon packets, with the photon position uncertainty of Δx. Film strip A and film strip B conceptually illustrate the digitized recordings of the reference and scattering beams, respectively. They are further processed with DSI operation to generate a spatiotemporal waterfall plot. **c,** Typical failure case of conventional interferometric detection: the photon packet arriving in the reference beam is generally incoherent with the backscatter of the target red photon packet, preventing effective interference. **d,** The unique condition that the backscatter of the target red photon packet can be demodulated: the reference beam provides a “twin” photon packet that is emitted simultaneously with the target red photon packet. LIGO: Laser Interferometer Gravitational-Wave Observatory. QC: quantum computing. QKD: quantum key distribution. EEG: Electroencephalography. OCT: optical communication terminal. OCIR: optical circulator. OC: optical coupler. PD: photodiode.

As each photon packet propagates along the fiber, it acts as an independent sensing probe and scans the entire link. Focusing on the red photon packet in Fig. 1b, when it travels along the fiber, perturbations at different positions are encoded into its Rayleigh backscattered signals. In this way, the CW broadband light carries out a distributed scan. However, at any instant, the Rayleigh scattering beam contains contributions from multiple positions along the link. This forms “scattering cluster” sequence, as depicted in Fig.1b, where backscatter from the red photon packet is mixed with that from other photon packets. In conventional DAS, detection is typically achieved by interfering the scattering beam with a reference beam. If this scattering cluster sequence (in Fig.1b) is detected in the same way, the backscatter of the red photon packet can be detected only when a mutually coherent photon packet in the reference beam arrives at the detector simultaneously. In most cases, as shown in Fig. 1c, such a mutually coherent counterpart is absent, and the sensing information carried by the backscatter of red photon packet cannot be retrieved. A unique case is shown in Fig. 1d: the photon packet arriving at the detector in reference beam is the twin of the red photon packet, meaning they are emitted simultaneously and are mutually coherent. However, when the red photon packet scans the fiber link, this unique case occurs only at a single instant and cannot realize distributed sensing. Therefore, for CW broadband light, a new sensing method is necessary.

If the photon packets in reference beam, and the scattering clusters in scattering beam can be recorded separately, the backscatter of the red photon packet can then be numerically interfered with its counterpart in reference beam, enabling distributed sensing along the entire link. As conceptually represented in Fig. 1b, the photon packet stream of reference beam is recorded on film strip A, and the scattering cluster sequence is recorded on film strip B. To extract the sensing information carried by a scattering cluster in a given frame of film strip B, film strip A can be scanned so that each photon packet recorded on it successively interferes with that scattering cluster. Repeating above operation to each frame of film strip B can achieve distributed sensing of the entire link. For clarity, a video of this process is provided in Supplementary Movie 1.

To achieve above concept, an auxiliary laser with superior phase stability is introduced to interfere with the reference beam and scattering beam separately, as shown in Fig. 2a. These two interference signals are denoted as $E_r(t)$ and $E_s(t)$, which correspond to film strips A and B in Fig. 1b. Then, the digital scanning interferometry (DSI) method we proposed in the Methods section is used to scan film strip A and achieve distributed sensing of the entire fiber link.

In our experiments, the H-DAS system in Fig. 2a uses two commercial optical communication terminals (Huawei S100-16T2S) as the transmit and receive nodes. At the transmitter, an SFP module launches broadband CW light carrying intensity-modulated data, with a power of ~0 dBm, into the 12 km fiber link. At the receiver, the data are recovered by direct detection. To enable sensing, a 99:1 optical coupler separates the SFP output into transmission beam (99%) and reference beam (1%). Rayleigh backscatter in the fiber link is guided out by an optical circulator. A narrow-linewidth laser module (NKT X15) serves as the auxiliary laser, with one output path interfering with the scattering beam to generate the scattering interference signal $E_s(t)$, and the other interfering with reference beam to form the reference interference signal $E_r(t)$. These two signals are applied to two I/Q demodulators referenced by the same oscillator (OSC), producing the in-phase (I) and quadrature (Q) outputs from each demodulator. These four channels are synchronously digitized by a data acquisition (DAQ) at 60 MHz and then processed using the DSI method, enabling distributed sensing along

the fiber link.

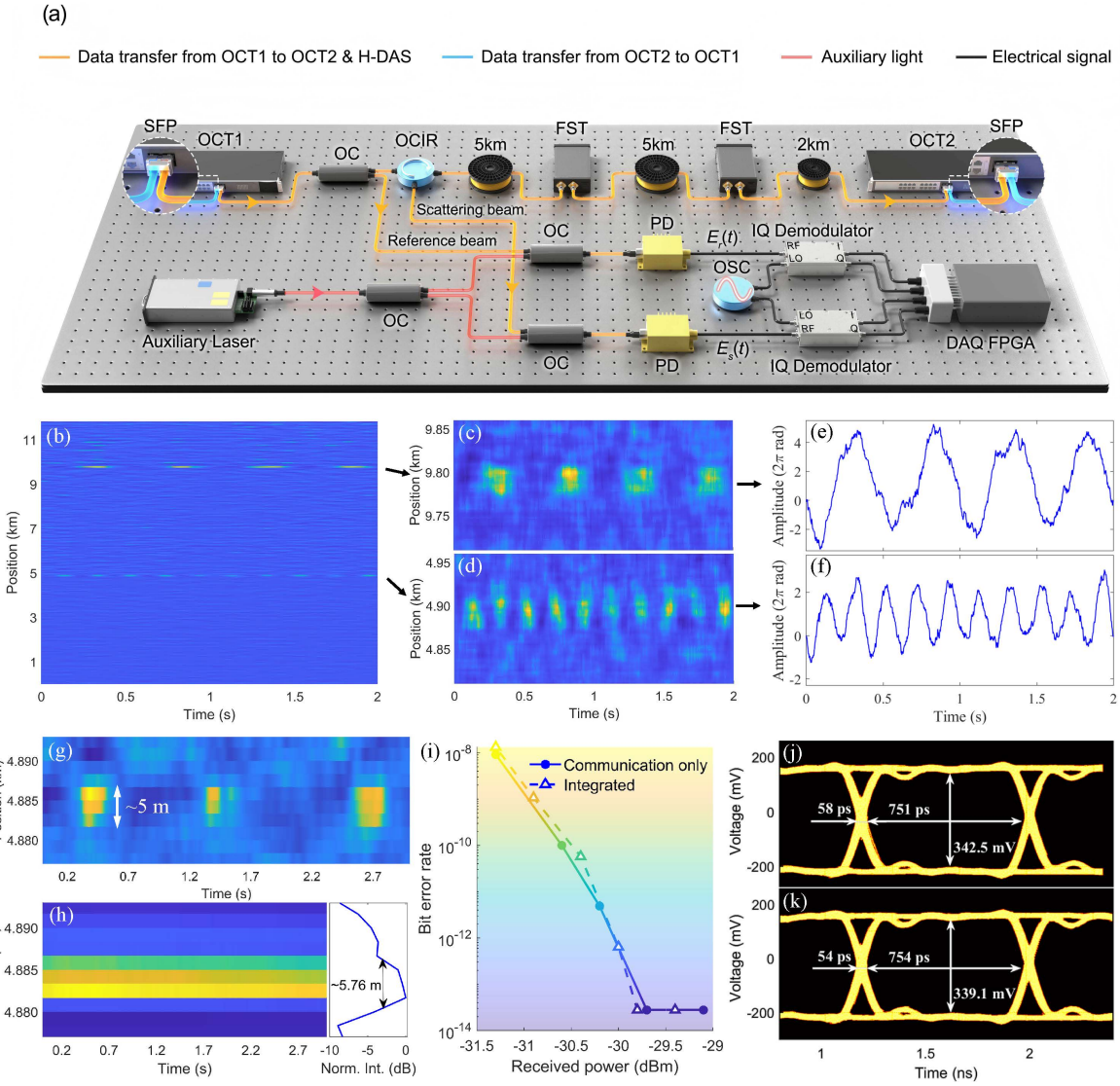


Fig. 2 | H-DAS system built on commercial optical communication terminals: integration of optical fiber communication and sensing. a, Experimental setup. Two commercial optical communication terminals (OCTs) serve as the transmit and receive nodes. The communication light from OCT1 to OCT2 (orange line) is directly reused as the sensing light to detect vibrations applied by two FSTs. An optical coupler (OC) splits the communication light into a transmission beam (99%) and a reference beam (1%), and an optical circulator (OCIR) extracts the scattering beam. An auxiliary laser (red line) is heterodyned with the reference beam and the scattering beam on two photodiodes (PDs), respectively. The resulting electrical signals (black line) are then processed by the IQ demodulators, DAQ and FPGA. **b,** Waterfall plot showing two controlled vibration events detected along the link. **c,** Zoom-in view of the 2 Hz vibration near 9.8 km. **d,** Zoom-in view of the 5 Hz vibration near 4.9 km. **e,** Time-domain waveform of the vibration near 9.8 km. **f,** Time-domain waveform of the vibration near 4.9 km. **g,** Waterfall plot for a point-like knocking

event. **h,** Waterfall plot for a point reflector and its FWHM. **i,** BER versus received optical power measured over 8 hours, comparing the communication-only case and the integrated communication-sensing case. **j,** Eye diagram without H-DAS integrated. **k,** Eye diagram with H-DAS integrated. FPGA: field-programmable gate array. Norm. Int.: normalized intensity.

To validate the distributed-sensing capability, two fiber stretchers (FSTs) are placed at 5 km and 10 km along the link, and are driven at 5 Hz and 2 Hz, respectively. The waterfall plot in Fig. 2b clearly resolves both vibrations, with zoomed-in views shown in Figs. 2c and 2d. In Fig. 2c, the 2 Hz vibration is localized to 9.78-9.80 km (spanning ~20 m), consistent with the ~20 m length of fiber wound inside the FST. The detected time-domain waveform is shown in Fig. 2e, with a peak-to-peak phase variation of ~7×2π rad. Similarly, in Fig. 2d, the 5 Hz vibration appears at 4.88-4.90 km (also spanning ~20 m), and the corresponding time-domain waveform in Fig. 2f exhibits a peak-to-peak phase variation of ~3×2π rad.

We further evaluate the spatial resolution of the SFP-based H-DAS system using two methods. First, we apply a point-like knocking vibration at ~5 km of the fiber (Supplementary Movie 2). The waterfall plot in Fig. 2g localizes the vibration event to 4.882-4.887 km, indicating a spatial resolution of ~5 m. Then we use a connector induced point reflection[39-41]. Fig. 2h (left) shows the measured reflected-intensity waterfall plot, where the reflector yields a localized response. By time-averaging the waterfall plot, Fig. 2h (right) shows a FWHM of ~5.76 m, indicating a spatial resolution of ~5 m. A more detailed discussion of the sensing spatial resolution is provided in the section “Physical mechanism of distributed sensing”.

To quantitatively evaluate the impact of distributed sensing on communication performance, the bit-error rate (BER) and eye diagram are measured using an optical communication test board, with and without H-DAS hardware integrated. Fig. 2i compares the measured BER under different received powers over 8-hour. The solid and dashed curves correspond to the systems without and with H-DAS, respectively. When the received power exceeds -29.5 dBm, the BER in both cases remains below 5×10^{-13}, and the two curves essentially overlap. Further, the eye diagrams for the two configurations are shown in Figs. 2j and 2k. Measurements are performed on a 1.25 Gbps intensity-modulation, with a 1 min acquisition time for each eye diagram. Quantitative comparison shows no observable

performance degradation: the eye widths (751 ps vs. 754 ps), jitter (58 ps vs. 54 ps), and eye heights (342.5 mV vs. 339.1 mV) remain nearly identical, indicating that integrating the H-DAS system has no measurable impact on communication quality.

Using the optical communication test board, the distributed sensing performance with and without data modulation is also evaluated. Similar results demonstrate that distributed sensing function is unaffected by data modulation (see Supplementary Note 1). The measured sensing sensitivity is essentially unchanged between the two cases, reaching ~2 nε/√Hz at 100 Hz and ~100 nε/√Hz at 1 Hz (see Supplementary Note 2).

Physical mechanism of distributed sensing

In the H-DAS system, the frequency uncertainty of the sensing light $\Delta\nu$ and the sensing spatial resolution ΔL form a pair of parameters constrained by the Heisenberg uncertainty principle, which provides the physical basis for distributed sensing. If both the backscattered and reference photons have a position uncertainty of Δx, after interference operation, the evaluated position uncertainty depends on their convolution result. For Gaussian distributions, the standard deviation of their convolution is $\sqrt{2}\Delta x$ [42]. Therefore, the spatial resolution (FWHM) of H-DAS system satisfies $\Delta L = \frac{1}{2}\cdot 2\sqrt{2\ln 2}\cdot\sqrt{2}\Delta x = 2\sqrt{\ln 2}\Delta x$ [18,37,42], from which their Heisenberg uncertainty relation can be written as:

$$\Delta L \cdot \Delta\nu \geq \frac{\sqrt{\ln 2}\nu_n}{2\pi} \quad (1)$$

To investigate this relation, lasers with different linewidths are employed, and their frequency uncertainty and sensing spatial resolution are measured, respectively. The frequency uncertainty $\Delta\nu$ of each laser is obtained by heterodyning it with the auxiliary laser (NKT X15, linewidth < 100 Hz)[43,44]. The achievable sensing spatial resolution ΔL is evaluated using the same reflector evaluation method described above[39-41].

As an example, for a laser with a linewidth of ~100 kHz, the heterodyne beat note is analyzed with a spectrum analyzer, and the beat spectrum is shown in Fig. 3a. Its FWHM is ~322 kHz, corresponding to the frequency uncertainty $\Delta\nu = FWHM/2\sqrt{2\ln 2} \approx 137$ kHz. Using this laser as the sensing light, the measured result in Fig. 3b shows a spatial resolution

of ~238 m. According to Eq. (1), for a frequency uncertainty of 137 kHz, the theoretical spatial resolution is $\Delta L \approx 193$ m. It is on the same order as the measured value of 238 m.

The relationship between frequency uncertainty $\Delta\nu$ and spatial resolution ΔL is further verified using two lasers with linewidths of ~1 kHz and ~4 kHz. For the ~1 kHz laser, the theoretical and measured spatial resolutions are ~62 km and ~82 km, respectively (Supplementary Figs. 1a, b). For the ~4 kHz laser, the corresponding values are ~15 km and ~16 km, respectively (Supplementary Figs. 1c, d). As shown in Fig. 3c, all measured points (red squares), except that of the SFP module (red horizontal bar), lie close to the theoretical curve given by Eq. (1). This interesting phenomenon warrants further discussion.

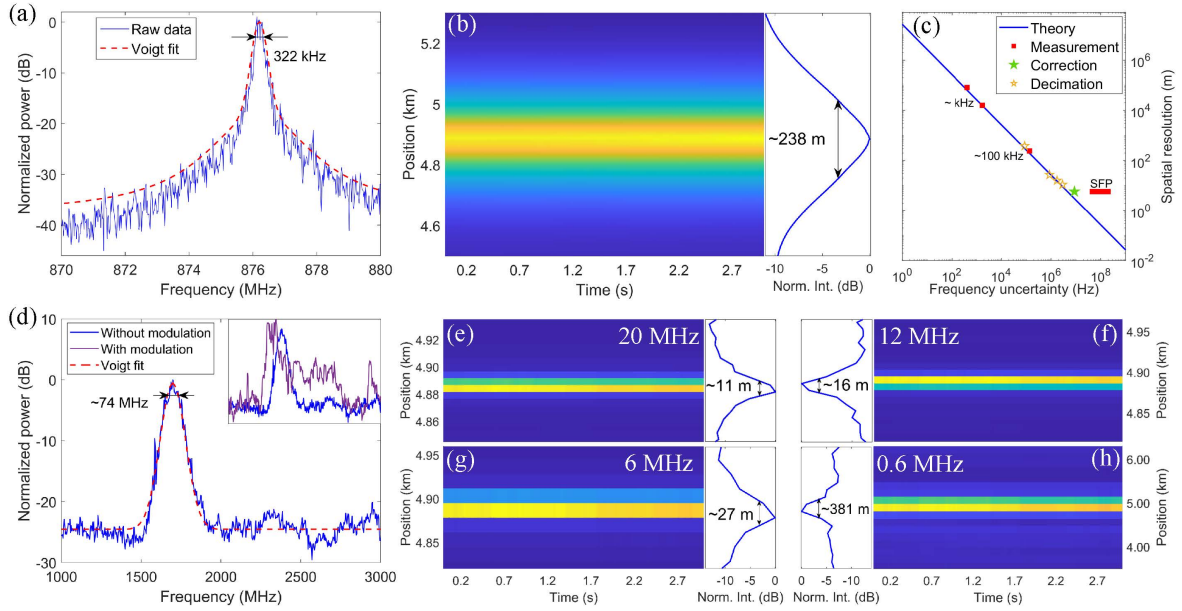


Fig. 3 | Uncertainty relation between the frequency uncertainty of sensing light and the sensing spatial resolution. a, Heterodyne beat spectrum between a laser with linewidth of ~322 kHz and the auxiliary laser. **b,** Waterfall plot and the corresponding spatial resolution obtained using the ~322 kHz-linewidth laser as the sensing source. **c,** The theoretical curve (blue line, from Eq. (1)) and experimental results for the sensing spatial resolution versus the frequency uncertainty of the sensing light. Red squares: measured points for ~kHz-linewidth and ~100 kHz-linewidth lasers. Red horizontal bar: measured result for the SFP module. Green star: corrected point considering the finite detection bandwidth and sampling rate when using SFP module. Orange open stars: measured points when using the SFP module under different decimated sampling rates. **d,** Heterodyne spectrum between the SFP and the auxiliary laser. Blue line: raw data without data modulation on SFP. Purple line: raw data with data modulation on SFP. **e–h,** Waterfall plots and the corresponding measured spatial resolution under different sampling rates when using SFP module. Norm.

Int.: normalized intensity.

The SFP module emits photons with large frequency uncertainty. Without data modulation, its heterodyne spectrum has a FWHM of ~74 MHz (Fig. 3d), corresponding to a frequency uncertainty of $\Delta\nu = 74\text{MHz}/2\sqrt{2\ln 2} \approx 31\text{MHz}$. With data modulation, its spectrum broadens further[45], as indicated by the purple curve in the inset of Fig. 3d. Therefore, we take 31 MHz as a lower bound for the frequency uncertainty of the SFP module and represent it in Fig. 3c by a red horizontal bar starting at 31 MHz. According to Eq. (1), frequency uncertainty of 31 MHz corresponds to a theoretical spatial resolution of ~0.9 m. However, the measured spatial resolution is ~5.8 m, as shown in Fig. 2h previously, which appears to deviate from the theoretical prediction.

In fact, this apparent discrepancy is consistent with the Heisenberg uncertainty principle: the attainable spatial resolution is limited by the measurable photon frequency uncertainty. Although the SFP emits photons with large frequency uncertainty, the finite acquisition bandwidth restricts the measurable portion of the spectrum. In the experiment, the acquisition system samples at 60 MHz and can only record signals with ~30 MHz bandwidth. Assuming a roughly uniform frequency distribution, according to the standard deviation of a uniform distribution[46], the maximum measurable frequency uncertainty is $\Delta\nu = 30\text{MHz}/\sqrt{12} \approx 8.7$ MHz. According to Eq. (1), the corresponding theoretical spatial resolution is ~3.0 m, reasonably close to the measured 5.8 m. The corrected point is marked by a green star in Fig. 3c.

When the sampling rate of acquisition system is further decimated to 20 MHz, the theoretical spatial resolution worsens to ~9 m. The measured value is ~11 m (Fig. 3e), reasonably consistent with the theoretical prediction and confirming that the spatial resolution is also governed by the acquisition capability. Figs. 3f-h present the measured spatial resolutions at further decimated sampling rates of 12 MHz, 6 MHz, and 0.6 MHz, respectively. The measured spatial resolutions of ~16 m, 27 m, and 381 m closely match the theoretical values of ~15 m, 30 m, and 305 m, respectively. These associated points are indicated by orange open stars in Fig. 3c and lie close to the theoretical curve, further confirming the consistency

with the Heisenberg uncertainty principle.

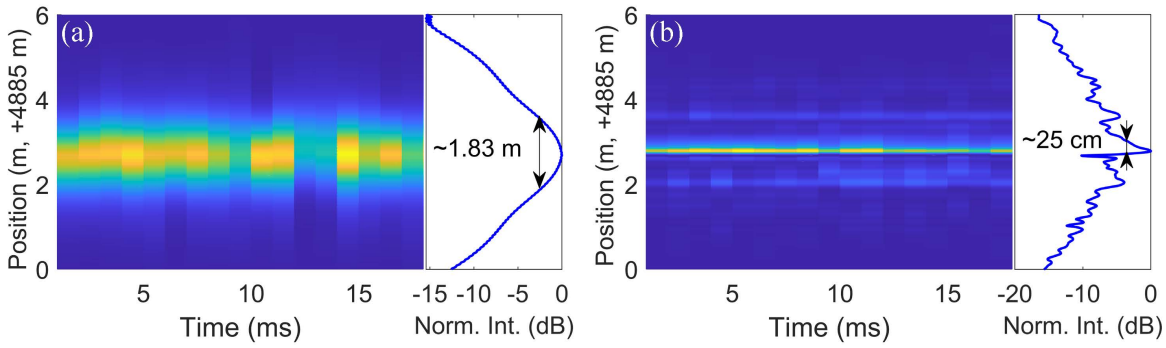


Fig. 4 | Measured sensing spatial resolution when using a high-speed digital oscilloscope for data acquisition. a, Waterfall plot and the corresponding spatial resolution obtained by SFP module without data modulation, yielding a spatial resolution of ~1.8 m. **b,** Waterfall plot and the corresponding spatial resolution obtained by SFP module with data modulation, improving the spatial resolution to ~25 cm.

To determine the spatial resolution achievable with the SFP module, we use a high-speed digital oscilloscope (RTO64). The oscilloscope provides a 4-GHz analog bandwidth, and records four channels at 10 GSa/s for 20 ms. Without data modulation, the measured spatial resolution is ~1.8 m (Fig. 4a), on the same order as the theoretical value of 0.9 m. With 1.25 Gbps data modulation, it improves significantly to 25 cm (Fig. 4b).

Field trial on high-speed railway

To further demonstrate the compatibility and sensing performance of the H-DAS system, it is deployed on a ~12 km trackside fiber link of the Beijing-Guangzhou high-speed railway between South Shawo Bridge and Dujiakan Bridge, as shown in Fig. 5a. A high-speed railway health-monitoring system has been established on this section previously[5]. When we replaced the previous monitor system by the H-DAS system operating with in-service optical communication terminals, train-induced vibrations and trajectories can be detected. Fig. 5b presents a 3500-s waterfall plot, where five upbound trains (from Dujiakan Bridge to South Shawo Bridge) and five downbound trains (from South Shawo Bridge to Dujiakan Bridge) are clearly distinguished. As a comparison, a conventional DAS system is connected to another fiber in the same cable to monitor the same section. The trajectories measured by H-DAS closely match those obtained by conventional DAS (Fig. 5c).

From 21 October 2025, the communication light is looped back at the remote end (South Shawo Bridge), effectively doubling the total fiber length to ~24 km. Fig. 5d shows the H-DAS sensing results over this extended span. The trajectories of high-speed trains remain clearly resolved over the entire 24 km link, and the results exhibit a symmetrical distribution centered at ~12 km. Between 1100 s and 1700 s, an additional vibration event appears near 6 km that is not associated with any high-speed train. This extra event is also captured by the conventional DAS, shown in Fig. 5e.

Field investigation reveals a large construction site adjacent to the high-speed railway at the experimentally located position. The official construction schedule (17 October 2025 to 3 February 2026) covers experimental period of Fig. 5d. This suggests that the extra vibration event was caused by construction activity. Supporting photographs of the site are provided in Supplementary Note 3.

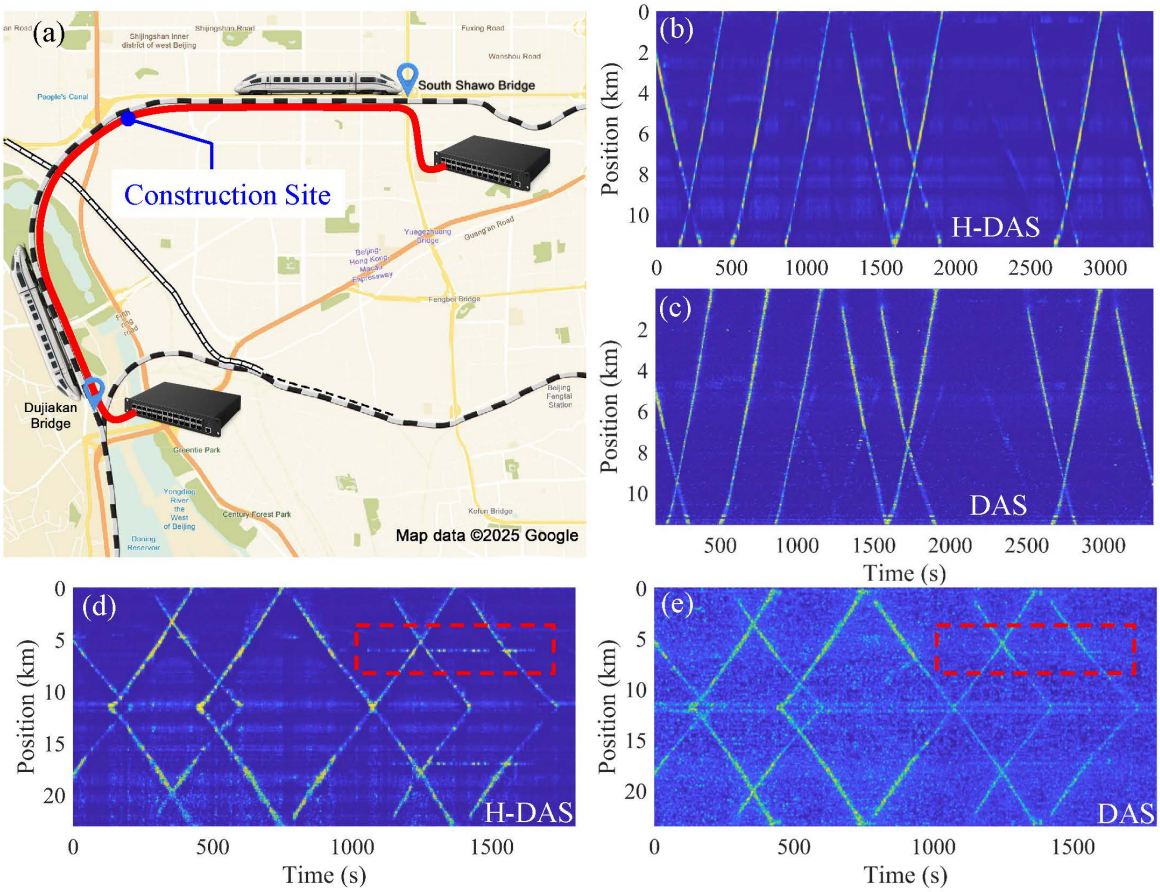


Fig. 5 | Field deployment of H-DAS system on Beijing-Guangzhou high-speed railway. a, The H-DAS system is deployed on an in-service trackside telecom cable between South Shawo Bridge and Dujiakan Bridge (total length ~12 km). The blue line marks a large construction site alongside the railway. **b,** Waterfall

plot from a continuous ~3500-s measurement by the H-DAS system, in which train trajectories are clearly resolved. **c,** Waterfall plot measured by a conventional DAS connected to another fiber in the same cable. **d,** Sensing results of the H-DAS system after looping back the light at South Shawo Bridge, extending the effective link length to ~24 km. The red dashed box highlights an extra vibration event near ~6 km during 1100-1700 s. **e,** Waterfall plot measured simultaneously by the conventional DAS system, showing the same extra vibration event near ~6 km.

Implications for distributed acoustic sensing

Realizing distributed sensing on existing fiber networks requires reusing installed cables and in-service communication terminals. Conventional techniques, including pulse modulation[6-12], frequency sweeping[25], and frequency-division multiplexing[18] have unlocked much of the deployed cable's potential, yet the communication light itself remains underutilized. This study demonstrates that low-cost, broadband CW light from communication SFP modules can serve as an effective distributed sensing source. This paves the way for integrating sensing capabilities directly into existing communication networks, and could ultimately contribute to a widely distributed "nervous system" on the Earth's surface.

Although this study establishes the physical basis and feasibility of H-DAS, future work can draw on performance-optimization methods from conventional DAS. Such research will be crucial for extending the sensing range, improving the signal-to-noise ratio, thereby enabling high-performance applications in fundamental science, smart cities, and geological monitoring. Supplementary Note 4 further discusses how related techniques can be adapted to H-DAS.

Acknowledgements: We acknowledge the support of Beijing Natural Science Foundation (L254064), and National Natural Science Foundation of China grant 62171249. We would like to thank Jianguo Zhao, Changan Liu and Wei Zheng of Beijing Railway Bureau, and Gongjian Hengye Communication Technology Corporation Limited for arranging the field deployment.

Author contributions: Z.P., C.L. and B.W. conceived and designed the experiments. B.W. supervised the project and led the collaborative efforts. Z.P., C.L, D.S., W.L., T.W., H.Z., P.S. and B.W. performed the experiments. Z.P., C.L. and B.W. analyzed the data and wrote the manuscript. All authors participated in the discussion and analysis of the manuscript.

Competing interests: The authors declare no competing interests.

Materials & Correspondence: Correspondence and requests for materials should be addressed to bo.wang@tsinghua.edu.cn.

Data availability: The data that support the findings of this study are available at Zenodo (https://doi.org/10.5281/zenodo.18382519), and will be made publicly available upon publication.

Code availability: The code used in this study is available at Zenodo (https://doi.org/10.5281/zenodo.18382519), and will be made publicly available upon publication.

References

1. Li, J., Kim, T., Lapusta, N., Biondi, E. & Zhan, Z. The break of earthquake asperities imaged by distributed acoustic sensing. *Nature* **620**, 800–806 (2023).
2. Li, J. et al. Earthquake focal mechanisms with distributed acoustic sensing. *Nat. Commun.* **14**, 4181 (2023).
3. Zhu, W. et al. Seismic arrival-time picking on distributed acoustic sensing data using semi-supervised learning. *Nat. Commun.* **14**, 8192 (2023).
4. Liu, J. et al. Urban sensing using existing fiber-optic networks. *Nat. Commun.* **16**, 3091 (2025).
5. Wang, G. *et al.* Laser interferometry for high-speed railway health inspection using telecom fiber along the line. *Nat. Commun.* **16**, 4129 (2025).
6. Jousset, P. *et al.* Fibre optic distributed acoustic sensing of volcanic events. *Nat. Commun.* **13**, 1753 (2022).
7. Biondi, E., Zhu, W., Li, J., Williams, E. F. & Zhan, Z. An upper-crust lid over the Long Valley magma chamber. *Sci. Adv.* **9**, eadi9878 (2023).
8. Atterholt, J. & Zhan, Z. Fine-scale Southern California Moho structure uncovered with distributed acoustic sensing. *Sci. Adv.* **10**, eadr3327 (2024).
9. Li, J. *et al.* Minute-scale dynamics of recurrent dike intrusions in Iceland with fiber-optic geodesy. *Science* **388**, 1189–1193 (2025).
10. Walter, F. *et al.* Distributed acoustic sensing of microseismic sources and wave propagation

in glaciated terrain. *Nat. Commun.* **11**, 2436 (2020).

11. Fichtner, A. *et al.* Hidden cascades of seismic ice stream deformation. *Science* **387**, 858–864 (2025).
12. Gräff, D. *et al.* Calving-driven fjord dynamics resolved by seafloor fibre sensing. *Nature* **644**, 404–412 (2025).
13. Marra, G. et al. Ultrastable laser interferometry for earthquake detection with terrestrial and submarine cables. *Science* **361**, 486–490 (2018).
14. Lindsey, N. J. et al. Illuminating seafloor faults and ocean dynamics with dark fiber distributed acoustic sensing. *Science* **366**, 1103–1107 (2019).
15. Zhan, Z. et al. Optical polarization-based seismic and water wave sensing on transoceanic cables. *Science* **371**, 931–936 (2021).
16. Williams, E. F. et al. Distributed sensing of microseisms and teleseisms with submarine dark fibers. *Nat. Commun.* **10**, 5778 (2019).
17. Marra, G. et al. Optical interferometry-based array of seafloor environmental sensors using a transoceanic submarine cable. *Science* **376**, 874–879 (2022).
18. Wang, J., Zhang, J., Lau, A. P. T. & Lu, C. Integrated ultra-large dynamic vibration sensing with fronthaul analog radio-over-fiber transmission. *Photon. Res.* **13**, 2339–2351 (2025).
19. Sun, X. *et al.* Genetic-optimised aperiodic code for distributed optical fibre sensors. *Nat. Commun.* **11**, 5774 (2020).
20. Soriano-Amat, M. *et al.* Time-expanded phase-sensitive optical time-domain reflectometry. *Light Sci. Appl.* **10**, 51 (2021).
21. Li, J. & Zhang, M. Physics and applications of Raman distributed optical fiber sensing. *Light Sci. Appl.* **11**, 128 (2022).
22. Wang, C. *et al.* Chaos Raman distributed optical fiber sensing. *Light Sci. Appl.* **12**, 213 (2023).
23. Youn, J. H. *et al.* Brillouin expanded time-domain analysis based on dual optical frequency combs. *Light Sci. Appl.* **13**, 149 (2024).
24. Ip, E. *et al.* Vibration Detection and Localization Using Modified Digital Coherent Telecom Transponders. *J. Lightwave Technol.* **40**, 1472–1482 (2022).
25. He, H. *et al.* Integrated sensing and communication in an optical fibre. *Light Sci. Appl.* **12**,

25 (2023).
26. Liu, S. *et al.* Integrated quantum communication network and vibration sensing in optical fibers. *Optica* **11**, 1762–1772 (2024).
27. Carver, C. J. & Zhou, X. Polarization sensing of network health and seismic activity over a live terrestrial fiber-optic cable. *Commun. Eng.* **3**, 91 (2024).
28. Mecozzi, A. *et al.* Geophysical sensing using Jones matrices extracted from submarine optical cable transceivers carrying live traffic. *Optica* **12**, 1712–1719 (2025).
29. The LIGO Scientific Collaboration. Enhanced sensitivity of the LIGO gravitational wave detector by using squeezed states of light. *Nat. Photonics* **7**, 613–619 (2013).
30. Clark, J. B., Lecocq, F., Simmonds, R. W., Aumentado, J. & Teufel, J. D. Observation of strong radiation pressure forces from squeezed light on a mechanical oscillator. *Nat. Phys.* **12**, 683–687 (2016).
31. del Campo, A., Egusquiza, I. L., Plenio, M. B. & Huelga, S. F. Quantum speed limits in open system dynamics. *Phys. Rev. Lett.* **110**, 050403 (2013).
32. Deffner, S. & Campbell, S. Quantum speed limits: from Heisenberg's uncertainty principle to optimal quantum control. *J. Phys. A: Math. Theor.* **50**, 453001 (2017).
33. Coles, P. J., Berta, M., Tomamichel, M. & Wehner, S. Entropic uncertainty relations and their applications. *Rev. Mod. Phys.* **89**, 015002 (2017).
34. Gabor, D. Acoustical quanta and the theory of hearing. *Nature* **159**, 591–594 (1947).
35. Oppenheim, J. N. & Magnasco, M. O. Human time-frequency acuity beats the Fourier uncertainty principle. *Phys. Rev. Lett.* **110**, 044301 (2013).
36. Moca, V. V., Bârzan, H., Nagy-Dăbâcan, A. & Mureșan, R. C. Time-frequency super-resolution with superlets. *Nat. Commun.* **12**, 337 (2021).
37. Qvarfort, S., Serafini, A., Barker, P. F. & Bose, S. Gravimetry through non-linear optomechanics. *Nat. Commun.* **9**, 3690 (2018).
38. Kudyshev, Z. A. *et al.* Machine learning assisted quantum super-resolution microscopy. *Nat. Commun.* **14**, 4828 (2023).
39. Denisov, A., Soto, M. A. & Thévenaz, L. Going beyond 1000000 resolved points in a Brillouin distributed fiber sensor: theoretical analysis and experimental demonstration. *Light Sci. Appl.* **5**, e16074 (2016).

40. Wan, A. *et al.* Co-channel multiplexing for Rayleigh-scattering-based information systems. *Sci. China Inf. Sci.* **68**, 182304 (2025).
41. Li, D. *et al.* Fading-suppressed Φ-OTDR with high spatial-resolution based on a chirped electro-optic frequency comb. *Opt. Express* **34**, 1451-1464 (2026).
42. Sterczewski, L. A. & Sotor, J. Two-photon imaging of soliton dynamics. *Nat. Commun.* **14**, 3339 (2023).
43. Pang, Z. *et al.* High-precision laser spectrum analyzer via digital decoherence. *Laser Photon. Rev.* **20**, e01773 (2026).
44. NKT Photonics A/S. *Koheras BASIK Datasheet* (2025). https://www.nktphotonics.com/wp-json/nktphotonics/v1/download/Koheras-BASIK/Koheras%20BASIK%20Datasheet.pdf (accessed 23 Jan 2026).
45. Villafranca, A., Lasobras, J. & Garcés, I. Precise characterization of the frequency chirp in directly modulated DFB lasers. In *Proc. 6th Spanish Conference on Electronic Devices* (CDE 2007), San Lorenzo de El Escorial, Madrid, Spain, 30 Jan-2 Feb 2007 (IEEE, 2007).
46. Uncertainty of measurement—part 3: guide to the expression of uncertainty in mea surement (GUM:1995). ISO/IEC Guide 98-3:2008. https://www.iso.org/standard/50461.html (International Organization for Standardization, 2008).

Methods

Digital scanning interferometry

For the H-DAS system shown in Fig. 2a, the detected heterodyne signals $E_s(t)$ and $E_r(t)$ can be written as:

$$E_s(t) = \int_{z=0}^{L} r(z) A\left(t - \frac{2z}{v_n}\right) \cos\left[\omega_0 t + \varphi\left(t - \frac{2z}{v_n}\right) + \varphi_z(t)\right] dz, \tag{2}$$

$$E_r(t) = A(t) \cos\left[\omega_0 t + \varphi(t)\right]. \tag{3}$$

Here, $E_s(t)$ contains the integrated contributions of scattering light from all positions along the fiber link at time t. $r(z)$ is the intensity coefficient of the backscattered light at position z. $A(t)$ and $\varphi(t)$ are the amplitude and phase fluctuations of the launched light. Constant branch-dependent coefficients (e.g., splitting ratios and detection gains) are omitted, as they only introduce an overall scaling and do not affect the phase demodulation. The parameter ω_0 is the angular frequency difference between the auxiliary and sensing lasers, which is ~2π×9 GHz in our experiments. The term $\varphi_z(t)$ represents the perturbation induced phase term at position z, and L is the length of the sensing fiber link. v_n is the velocity of light in the fiber, here $v_n = c/n$, with c the velocity of light in vacuum and n the refractive index of the fiber.

Two detected heterodyne signals are fed into the RF input of two IQ demodulators of Fig. 2a. To extract their phase information, a 9 GHz signal from the OSC of Fig. 2a serves as the LO input of both IQ demodulators, yielding four outputs:

$$S_{sI}(t) = \int_{z=0}^{L} r(z) A\left(t - \frac{2z}{v_n}\right) \sin\left[\varphi\left(t - \frac{2z}{v_n}\right) + \varphi_z(t)\right] dz, \tag{4}$$

$$S_{sQ}(t) = \int_{z=0}^{L} r(z) A\left(t - \frac{2z}{v_n}\right) \cos\left[\varphi\left(t - \frac{2z}{v_n}\right) + \varphi_z(t)\right] dz, \tag{5}$$

$$S_{rI}(t) = A(t) \sin\left[\varphi(t)\right], \tag{6}$$

$$S_{rQ}(t) = A(t) \cos\left[\varphi(t)\right]. \tag{7}$$

Next, $S_{rI}(t)$ and $S_{rQ}(t)$ are time-shifted by a programmable delay τ. They are then combined with $S_{sI}(t)$ and $S_{sQ}(t)$ as shown below, generating a new quadrature pair $S_I(t)$ and $S_Q(t)$:

$$\begin{aligned} S_I(t) &= S_{sI}(t)\cdot S_{rQ}(t-\tau) - S_{sQ}(t)\cdot S_{rI}(t-\tau) \\ &= \int_{z=0}^{L} r(z)\, A\left(t-\frac{2z}{v_n}\right) A(t-\tau) \sin\left[\varphi\left(t-\frac{2z}{v_n}\right) - \varphi(t-\tau) + \varphi_z(t)\right] dz, \end{aligned} \tag{8}$$

$$\begin{aligned} S_Q(t) &= S_{sQ}(t)\cdot S_{rQ}(t-\tau) + S_{sI}(t)\cdot S_{rI}(t-\tau) \\ &= \int_{z=0}^{L} r(z)\, A\left(t-\frac{2z}{v_n}\right) A(t-\tau) \cos\left[\varphi\left(t-\frac{2z}{v_n}\right) - \varphi(t-\tau) + \varphi_z(t)\right] dz. \end{aligned} \tag{9}$$

More specifically, taking Eq. (9) as an example, the integral includes contributions from scattering light at all positions along the fiber link. For a given scanning delay $\tau=\tau_0$, only the scattering light from the vicinity of $z_0 = \frac{v_n \cdot \tau_0}{2}$ (within the spatial resolution of $\pm\frac{\Delta L}{2}$, which is defined in Eq. (1)) produces a phase-stable interference term. This term can be approximated as $r\left(\frac{v_n\tau_0}{2}\right) A^2(t-\tau_0)\cos\left[\varphi_{v_n\tau_0/2}(t)\right]$. Scattering light from other positions contributes like white noise, because the residual phase term $\varphi\left(t-\frac{2z}{v_n}\right) - \varphi(t-\tau_0)$ cannot be cancelled and fluctuates rapidly in time. By time-averaging $S_I(t)$ and $S_Q(t)$ over an appropriate window, these noise contributions can be effectively suppressed. Consequently, for an arbitrary delay τ, only the scattering light within the spatial region centered at $z = \frac{v_n \cdot \tau}{2}$ and of width $\pm\frac{\Delta L}{2}$ is preserved, while contributions from other locations are averaged out. In this case, after time-averaging operation, we can get:

$$\overline{S_I(t)} = r(z)\overline{A(t-\tau)\, A\left(t-\frac{2z}{v_n}\right)} \sin\left[\varphi_z(t)\right] = r\left(\frac{v_n\tau}{2}\right)\overline{A^2(t-\tau)} \sin\left[\varphi_{v_n\tau/2}(t)\right], \tag{10}$$

$$\overline{S_Q(t)} = r(z)\overline{A(t-\tau)\, A\left(t-\frac{2z}{v_n}\right)} \cos\left[\varphi_z(t)\right] = r\left(\frac{v_n\tau}{2}\right)\overline{A^2(t-\tau)} \cos\left[\varphi_{v_n\tau/2}(t)\right]. \tag{11}$$

In our experiments, the averaging time is set to 1 ms, corresponding to 60,000 samples

and yielding a noise power reduction of ~48 dB[47]. Finally, by applying phase demodulation operation to the averaged quadrature signals[48,49], as described in Eq. (12), the sensing information $\varphi_{v_n\tau/2}(t)$ at position $z=\frac{v_n\tau}{2}$ can be recovered:

$$\varphi_{v_n\tau/2}(t)=\arctan\left[\frac{\overline{S_I(t)}}{\overline{S_Q(t)}}\right], \tag{12}$$

and the scattering intensity $A_{v_n\tau/2}(t)$ at position $z=\frac{v_n\tau}{2}$ is obtained as:

$$A_{v_n\tau/2}(t)=\sqrt{\overline{S_I(t)}^2+\overline{S_Q(t)}^2}=r(\frac{v_n\tau}{2})\overline{A^2(t-\tau)} \tag{13}$$

47. Vepsäläinen, A. *et al.* Improving qubit coherence using closed-loop feedback. *Nat. Commun.* **13**, 1932 (2022).
48. Corbella, I., Martín Neira, M., Vilaseca, R., Catalan, A., Torres, F. & Suess, M. A novel digital IQ demodulation for interferometric radiometers. *Remote Sens.* **13**, 1156 (2021).
49. Li, C., Pang, Z., Wang, G., Wang, F., Dai, H., Li, W. & Wang, B. A digital phase resolving method for fiber optic sensing. *J. Lightwave Technol.* **42**, 7384–7395 (2024).

Supplementary Files

This is a list of supplementary files associated with this preprint. Click to download.

- SupplementaryNote.pdf
- SuppleVideo1.mp4
- SuppleVideo2.mp4